Evaporation kinetics of pure water drops: thermal patterns, Marangoni flow and interfacial temperature difference

Tejaswi Josyula,[1] Zhenying Wang,[2] Alexandros Askounis,[2,3] Daniel Orejon,[2] Sivasankaran Harish,[2] Yasuyuki Takata,[2,4] Pallab Sinha Mahapatra,[1] and Arvind Pattmatta[1,*]

[1] *Department of Mechanical Engineering,Indian Institute of Technology Madras,600036,India*
[2] *International Institute for Carbon-Neutral Energy Research (WPI-I2CNER), Kyushu University, 744 Motooka, Nishi-ku, Fukuoka 819-0395, Japan*
[3] *Engineering, Faculty of Science, University of East Anglia, Norwich, NR5 7TJ, United Kingdom*
[4] *Department of Mechanical Engineering, Kyushu University, 744 Motooka, Nishi-ku, Fukuoka 819-0395, Japan*

(Dated: August 29, 2018)

We report a systematic study on the role of Marangoni convection on the evaporation kinetics of pure water drops, considering the influence of heating regime and surface wettability. The Marangoni flows were induced via heating under constant wall temperature (uniform heating) and constant heat flux (local heating) regimes below the drops. To visualize the thermal patterns/flows emerging within the water drops we employed infrared (IR) thermography and we captured the evolution of the drop profile with a CCD camera to follow the evaporation kinetics of each drop. We observed a strong correlation between the temperature difference within the drop and the evolution of drop shape during different modes of evaporation (*i.e.* constant radius, angle or stick-slip) resulting in different Marangoni flow patterns. Under uniform heating, stable recirculatory vortices due to Marangoni convection emerged at high temperature which faded at later stages of the evaporation process. On the other hand, in the localized heating case, the constant heat flux resulted in a rapid increase of the temperature difference within the drop capable of sustaining Marangoni flows throughout the evaporation. Surface wettability was found to also play a role in both the emergence of the Marangoni flows and the evaporation kinetics. In particular, recirculatory flows on hydrophobic surfaces were stronger when compared to hydrophilic for both uniform and local heating. To quantify the effect of heating mode and the importance of Marangoni flows, we calculated the evaporative flux for each case and found to it to be much higher in the localized heating case. Evaporative flux depends on both diffusion and natural convection of the vapor phase to the ambient. Hence, we estimated the Grashof number for each case and found a strong relation between natural convection in the vapor phase and heating regime or Marangoni convection in the liquid phase. Subsequently, we demonstrate the limitation of current diffusion-only models describing the evaporation of heated drops.

I. INTRODUCTION

Sessile drop evaporation is of interest in academic and industrial research owing to applications such as ink jet printing [1], biological and chemical assays [2], thin film coatings [3], DNA depositions [4], efficient electronic cooling, etc [5]. For a typical sessile drop evaporating into an unsaturated atmosphere, Picknett and Bexon [6] identified two different modes of evaporation; one at constant contact radius with a decrease in contact angle (CCR) and the second one at constant contact angle while the contact radius recedes (CCA). The authors also observed a mixed mode at the end of the evaporation where a simultaneous decrease in both contact radius and contact angle occurred. The kinetics of evaporation and the change in mass or volume during evaporation are greatly dependent on these distinct modes of evaporation. For instance, CCR mode of evaporation with linearly decreasing drop weight/volume is reported on a wetting surface (water on glass) with a contact angle less than 90˚[7]. On the other hand, on a non-wetting surface (water on Teflon) with a contact angle greater than 90˚, the CCA mode of evaporation is reported and the decrease in weight/volume is observed to be non-linear. Further, the decrease in volume according to a power law is reported for drops evaporating on hydrophobic and superhydrophobic surfaces [8, 9]. Apart from the extreme modes of evaporation (CCR and CCA), a stick-slip mode of evaporation with repetitive cycles of stick and slip of the contact line is observed for pure fluids [10] and also for colloidal suspensions [11]. The strong influence of substrate wettability [8, 12], shape of the sessile drop [13], ambient conditions [14–16] and substrate properties [17, 18] on the evaporation process are extensively reported.

For a sessile drop in contact with a solid substrate, the evaporative flux at the liquid-vapor interface is non-uniform and depends on the drop shape [19]. The evaporative flux is higher near the contact line for drops with contact angles less than 90˚, whereas for drops with contact angles greater than 90˚it is higher at the apex [9, 20]. This non-uniformity in evaporative flux gives rise to temperature differences inside the drop due to evaporative cooling induced by the release of latent heat of vaporiza-

* arvindp@iitm.ac.in

tion. Besides evaporative cooling, on a heated substrate, the temperature difference inside the drop additionally arises due to the thermal resistance imposed by liquid thickness. These phenomena can cause internal fluid motion either due to buoyant convection or Marangoni convection. For example, the presence of buoyant convection is attributed to recirculating vortices reported in hanging methanol drops [21]. Elsewhere, prominent Marangoni recirculatory flow from the triple contact line to the apex in volatile octane drops is observed to fully counteract the well-known capillary flow [22]. In evaporating drops, capillary flow is defined as the flow from the center of the drop towards the triple contact line (TCL) induced to replenish the evaporating liquid at the triple contact line [23]. Moreover, hydrothermal waves (HTWs) arising due to Marangoni stresses traveling azimuthally from center to the edge of the drop are observed in evaporating alcohol drops [24, 25]. Numerous experimental and theoretical studies are recently reported aiming for a further understanding of the physical mechanisms of mentioned HTWs and Marngoni flows within evaporating drops [14, 26, 27].

Although drop evaporation is a ubiquitous phenomenon widely studied, experimental observations of the internal flows inside pure water drops remain scarce. The previously reported absence of Marangoni flow in pure water drops evaporating at ambient temperature is presumably due to surface contamination [22]. However, another study using confocal microscopy reported the presence of Marangoni flow in evaporating drops at ambient temperature [28]. Hence, the absence of Marangoni flows in pure water drops cannot be solely explained by the presence of contaminants. Further, deposition patterns from an evaporating water drop containing colloidal particles are reported to be significantly altered in the presence of substrate heating [29], due to Marangoni currents, although no visualization of convective patterns is reported [29]. Elsewhere, a laser is used to locally heat the substrate below the center and edge of pure water drops inducing thermal gradients and, in turn, recirculating twin vortices, which is attributed to Marangoni convection [30, 31]. In addition to internal fluid motion during evaporation, for evaporating drops on heated substrates, the difference in temperature between the substrate, the drop and the ambient induces natural convection in the vapor phase. This natural convection in the vapor phase is cited as the reason for the enhanced evaporation rate in experiments when compared to those predicted by the diffusion model [32–35]. Nonetheless, the presence and visualization of Marangoni convection in pure water drops is still an open debate and a systematic study to observe the convective patterns with a non-intrusive measurement and visualization is scarce in the literature.

The focus of the present study is to investigate the effect of Marangoni convection on the evaporation kinetics of pure water drops, considering different substrate heating regimes viz. heating the substrate uniformly (constant wall temperature) and heating the substrate locally (constant heat flux) and wettabilities. We note here that a previous work reported Marangoni flows in pure water drops on locally heated substrates [30, 31]. However, no comparison of the mechanism inducing Marangoni convection in pure water drops depending on the heating mode was drawn yet. By systematically studying the evaporation of water drops under different heating modes, we probe interesting differences in the evaporation kinetics. We then attempt to quantify the influence of the observed Marangoni flows on the evaporation kinetics by demonstrating the limitation of current diffusion-based model and linking with natural convection of the vapor phase to the ambient.

II. EXPERIMENTAL SETUP AND METHODOLOGY

Schematic illustrations of the experimental setup for uniform heating and local heating are represented in Fig. 1a and Fig. 1b, respectively. In Fig. 1a, an aluminum heater block connected to a thermostatic bath maintains the surface at a constant temperature. The heater block is mounted on a scissor bench of adjustable height. Uniform heating is confirmed by measuring the temperature with four thermocouples inserted few millimeters below the surface at four different locations. For the case of uniform heating, two different substrate temperatures of 30 °C and 80 °C are investigated. Prior to drop deposition, the substrate is placed on the heater for several minutes until the substrate reaches the target temperature, which is confirmed with an additional thermocouple. A calibrated micropipette is used to dispense drops of 5.2 ± 0.3 μl. Drop shape during evaporation is captured from the side by a charge coupled device (CCD) Sentech (STC-MC152USB, resolution of 10 μm/px). An infrared (IR) camera FLIR SC4000 (temperature resolution of 18 mK and 3 μm to 5 μm spectral range) placed on top is used to record the spatiotemporal evolution of the thermal patterns at the drop liquid-vapor interface. To study the effect of wettability, a hydrophilic smooth silicon substrate (contact angle of water ca. 77°) and a hydrophobic silicon wafer coated with a thin layer of Cytop (water contact angle of ca. 113°) are used. Images are acquired at a constant frame rate of 4.8 and 30 fps for the CCD and for the IR camera, respectively. For all studied drops, the characteristic length, i.e., drop radius, is smaller than the capillary length $l_c = \sqrt{\frac{\gamma}{\rho g}}$ ($\sim$ 2.7 mm for water) and hence, volume and contact angle of the drops are calculated using spherical cap assumption. To impose local heating on the drop, an Integra-MP-30W diode laser (Spectra-Physics, 808 nm wavelength) with a spot size of $0.3 - 0.4$ mm, operating in continuous wave mode radiates/heats the substrate directly below the center of the drop. The power of the laser measured with a laser power meter (Vega, Ophir Optronics Solu-

tions Ltd.) is kept constant at 1.8 W. Locally heating the substrate is expected to result in a non-uniform temperature field on the substrate which changes with time unlike the constant substrate temperature on the uniformly heated substrates. To understand the characteristics of local heating and substrate temperature distribution, additional experiments are conducted by locally heating the substrate in the absence of a drop. The substrate temperature distribution under local heating in the absence of a drop is imaged within the calibrated range of the IR camera from 0 - 100 °C, i.e., for the first 13 seconds. As drops typically evaporate over longer timescales, we conduct numerical simulations using COMSOL 5.2 in order to extract the temperature evolution of the locally heated substrate over time. Details of the geometry, initial conditions, boundary conditions and results are presented in Appendix. Good agreement is observed between the experimental and simulation results as shown in Fig. 9d. A temperature difference of c.a. 6.5 °C is observed between the center of the hot spot and a distance 1.6 mm away from the center, which is typically the initial radius of our drops evaporating on a hydrophilic substrate. The temperature of the hot spot increases continuously to a value higher than that on uniform heating case at 80 °C . This demonstrates that the heat available below the drop is higher in the locally heated case. However, to be able to compare to some extent the two heating modes, the laser power is chosen so as to induce a similar maximum temperature at the drop liquid-vapor interface in both cases. Image processing and extraction of the drop profile evolution over time (radius, contact angle and volume) as well as the temperature distribution along the interface from IR snapshots are processed using MATLAB [36]. Experiments are carried out in controlled laboratory conditions where the ambient temperature and relative humidity are $17-18$ °C and $30-35$ %, respectively. We note here that the water temperature before drop deposition is that of the ambient. Satisfactory repeatability is achieved with maximum errors in contact angle, radius, and volume of $\pm 3^{\circ}$, 7%, and 12%, respectively.

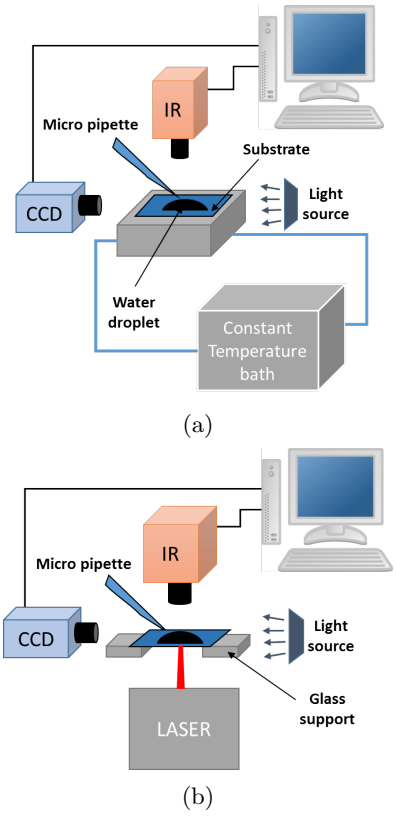

FIG. 1: Schematic of experimental setup for (a) uniform heating and (b) local heating scenarios.

III. RESULTS AND DISCUSSION

In this section, the results of the experimental investigations on the evaporation of pure water drops are discussed in terms of the evolution of drop shape parameters and the thermal patterns at the drop liquid vapor-interface. Distinctive stages in the temporal evolution of the contact angle and the contact radius are presented along with the evolving thermal patterns at the liquid-vapor interface. The variation of the evaporative flux averaged over the entire liquid-vapor drop interface with time in turn related to the evaporation mode, is also presented. Moreover, relevant non-dimensional numbers are deduced to understand the origin of the convective flows. Lastly, prediction of volume evolution by diffusion-based model and comparison with experimental observations are reported.

A. Evaporation on uniformly heated substrates at low temperature

For the cases of uniform heating at low substrate temperature of 30 °C, the kinetics of evaporation are shown in Fig. 2. The temporal evolution of contact angle and normalized contact radius (normalized by initial contact radius) are plotted for both hydrophilic (Fig. 2a) and hydrophobic (Fig. 2b) surfaces. Characteristic snapshots of the drop shape are included as top insets. In addition, the corresponding IR snapshots of the thermal patterns are shown as insets within both figures. Overall, the contact line dynamics follow three distinct stages on both surfaces. On a hydrophilic surface, as shown in Fig. 2a, the evaporation in Stage 1 proceeded with pinning of the triple contact line and decreasing contact angle (CCR mode). CCR is then followed by Stage 2 where evaporation takes place with a virtually constant contact angle at $63^{\circ}\pm 3^{\circ}$and the almost linear receding of the triple contact line. Towards the end of this stage, minor stick and slips of contact line leads to small jumps in contact angle which differs slightly from the traditional CCA mode of evaporation reported [11]. Eventually, evaporation enters Stage 3 where both contact radius and contact angle

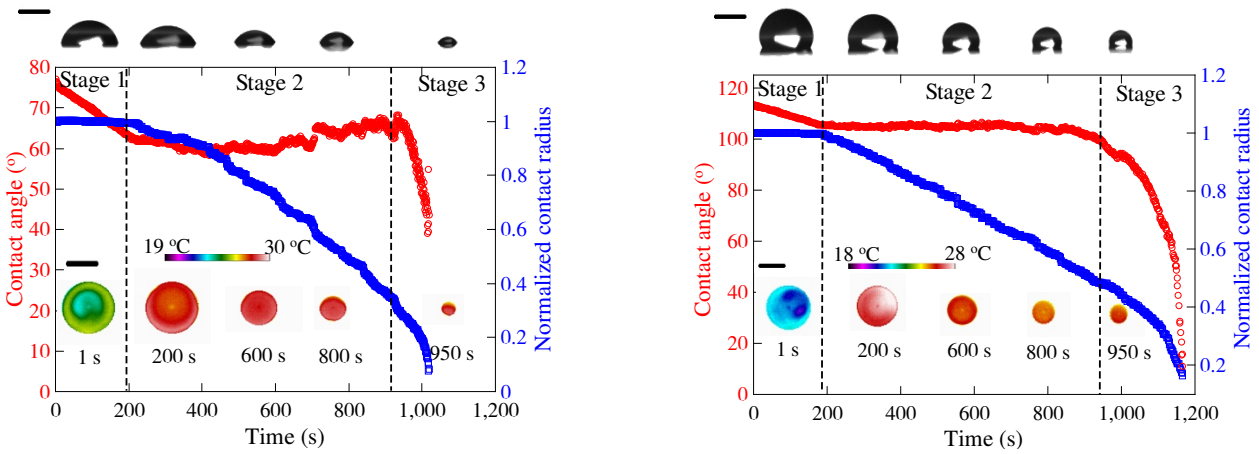

FIG. 2: Temporal evolution of contact angle and normalized contact radius on uniformly heated (a) hydrophilic and (b) hydrophobic surface at 30 °C. The three different evaporation stages can be readily identified by dashed lines. CCD snapshots from the side and IR thermography from the top are shown in insets. Scale bar is 1 mm.

decrease in a mixed mode of evaporation. On the other hand, on a hydrophobic surface (Fig. 2b), the evaporation takes place in the CCR mode, i.e., the contact angle decreases while the triple contact line remains pinned, for Stage 1. Subsequently, Stage 2 proceeds in the CCA mode with a constant contact angle of 104°±3°, which is then followed by the mixed mode of evaporation in Stage 3.

Closer inspection of IR thermography images on a hydrophilic and on a hydrophobic substrate (insets of Fig. 2a and 2b) unveil a cold spot at the liquid-vapor interface emerging approximately 1 s after the drop deposition. The corresponding IR thermography movies for hydrophilic and hydrophobic case can be viewed as supplementary videos SI.1 and SI.2, respectively [37]. When a drop at ambient temperature is placed on the heated substrate, the liquid just above the substrate will be heated first while the liquid at the apex remains colder. This temperature difference between the bottom and the apex of the drop can cause either buoyancy or thermocapillary convection inside the drop. As the surface tension of water varies inversely with temperature, the hotter liquid will try to move towards the colder region owing to its comparatively lower surface tension, giving rise to the twin vortices observed. The fact that the observed thermal patterns are also liquid patterns was experimentally elucidated by observing the motion of microparticles suspended in an evaporating pure water drop [30]. Nonetheless, at low substrate temperature, the temperature difference across the drop is small hence the convective cells faded longer period of evaporation. Since the difference between the ambient, the drop and the substrate temperature is low, the drop reaches thermal equilibrium, as portrayed by the uniform profile reported in the IR images. Detailed discussion on the prevailing interfacial temperature difference and its variation is presented in following sections.

B. Evaporation on uniformly heated substrates at high temperature

The temporal evolution of contact angle and normalized contact radius on the uniformly heated substrate at 80 °C is shown in Fig. 3. On a hydrophilic surface (Fig. 3a), similar to the case of low temperature heating at 30 °C, in Stage 1 evaporation takes place in the CCR mode, followed by a virtually constant contact angle (CCA mode) in Stage 2. In Stage 3, contact angle starts to decrease and almost at the end of evaporation the abrupt decrease in contact radius accompanied by an increase in contact angle is observed. For the case of evaporation on a hydrophobic surface (Fig. 3b), Stage 1 takes place in the CCR mode and is then followed by the CCA mode in Stage 2. At the end of Stage 2, a slip of contact line ensues followed by the final stage with a mixed mode of evaporation.

Focusing our attention on the IR snapshots, we can readily identify the emergence of twin vortices right after the drop deposition. At a substrate temperature of 80 °C, right after drop deposition, there is an initial temperature difference between the heated substrate and drop initially at ambient temperature, which induces the cold spot at the drop apex. At high substrate temperature, temperature difference inside the drop is governed by the interplay between evaporative cooling and the thermal resistance of the liquid through the drop. This results in an appreciable temperature difference inside the evaporating drop causing convective flows and movement of twin vortices throughout 60% to 80% of the drop lifetime. The behavior of the twin vortices at 80 °C is opposite to that observed at 30 °C where convective cells are noticeable

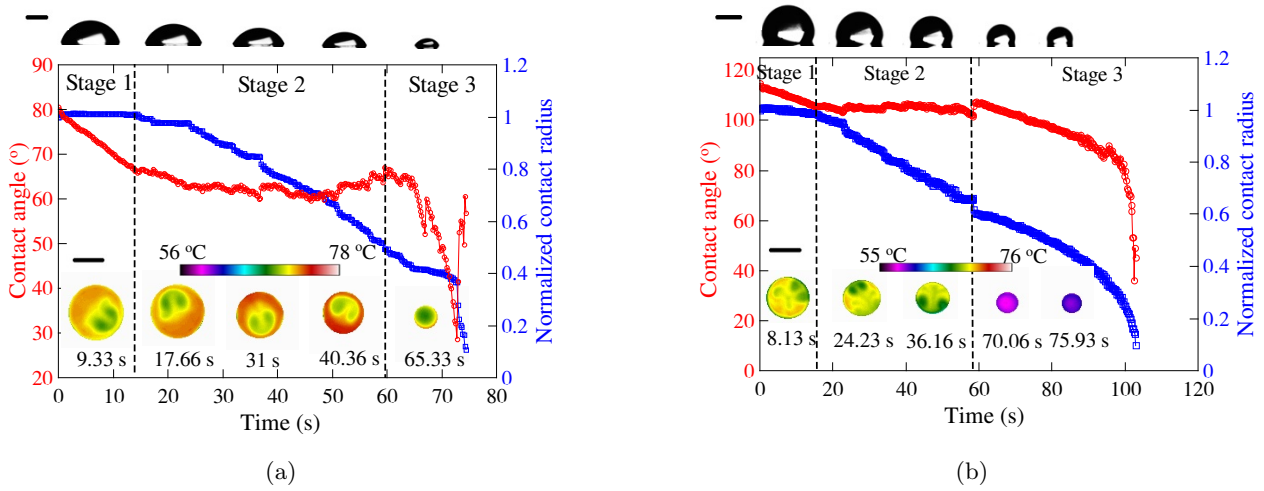

(a) (b)

FIG. 3: Contact angle and normalized contact radius evolution on uniformly heated (a) hydrophilic and (b) hydrophobic surfaces at 80 °C. The three different evaporation stages can be readily identified by dashed lines. CCD snapshots from the side and IR thermography from the top are shown in insets. Scale bar is 1 mm.

only at the beginning of evaporation and as the temperature of the drop is homogenized, convective cells are seen not to be stable.

The temporal evolution of thermal patterns at 80 °C is shown in insets of Fig. 3a and Fig. 3b for hydrophilic and hydrophobic surfaces, respectively (The corresponding IR thermography movies for hydrophilic and hydrophobic case can be viewed as supplementary videos SI.3 and SI.4, respectively [37]). During the initial stages of evaporation, i.e., Stage 1 and Stage 2, on a hydrophilic substrate (Fig. 3a) vigorous motion of the twin vortices and the shift of the vortices from one hemisphere to another is observed. This occurs due to the force exerted by the hot fluid moving towards the cold spot. The movement of twin vortices is the response of the system trying to attain thermal equilibrium and to homogenize the temperature distribution. The dominance of Marangoni convection in the observed convective flows is discussed and supported using relevant non-dimensional analysis in Section III E. On other hand, on a hydrophobic surface (Fig. 3b), during the first two stages of evaporation the continuous oscillating merging and splitting of the twin vortices ensues. Moreover, observing the evolving thermal patterns clearly suggested a more rapid movement of convective cells on a hydrophobic surface compared to a hydrophilic surface, which is further supported by the Marangoni numbers in Section III E. The higher thermocapillary currents on a hydrophobic surface can result from the higher liquid-vapor interface area due to the nature of drop curvature when compared to a hydrophilic surface. Further, the characteristic heat conduction path (drop's height) and the associated thermal resistance of liquid is higher compared to hydrophilic surfaces resulting in higher temperature differences between the bottom and the apex of the drop. Thereafter, in Stage 3, a sudden decrease of contact angle causes mixing of liquid inside of the drop homogenizing the surface temperature and hindering the convective patterns. This is attributed to the momentary increase in thermocapillary currents inside the drop when the drop enters the last stage of evaporation with decrease in both contact radius and contact angle [38]. In Stage 3 the temperature is almost uniform and no convective cells are seen. In the high temperature uniform heating case, the difference of temperature between the substrate, the drop and the ambiance will induce natural convection in the gas phase, which in turn will enhance the evaporation rates [32, 33].

The above results provide the experimental evidence of recirculating vortices in pure water drops on both hydrophilic and hydrophobic substrates heated uniformly.

C. Evaporation on locally heated substrates

To further interpret the convective flows in evaporating pure water drops, we also address the effect of locally heating the substrate, which can be considered as a constant heat flux case. To achieve constant heat flux condition, we used a laser to locally heat the substrate directly below the center of the drops, similar to a previous report [31]. Care is taken to control the power of the laser aiming to induce the same maximum temperature at the drop liquid-vapor interface as in the case of high temperature uniform heating. The temporal evolution of contact radius and contact angle on a hydrophilic and on a hydrophobic surface is presented in Fig. 4a and 4b, respectively. In both cases, the drop evaporation initially occurs in the CCR mode for Stage 1, followed by CCA during Stage 2. Here, Stage 3 of evaporation takes place in a stick-slip mode. It is worth noticing that compared to the case of uniform heating, in Stage 3, the number of stick-slip events are greater on the hydrophilic sur-

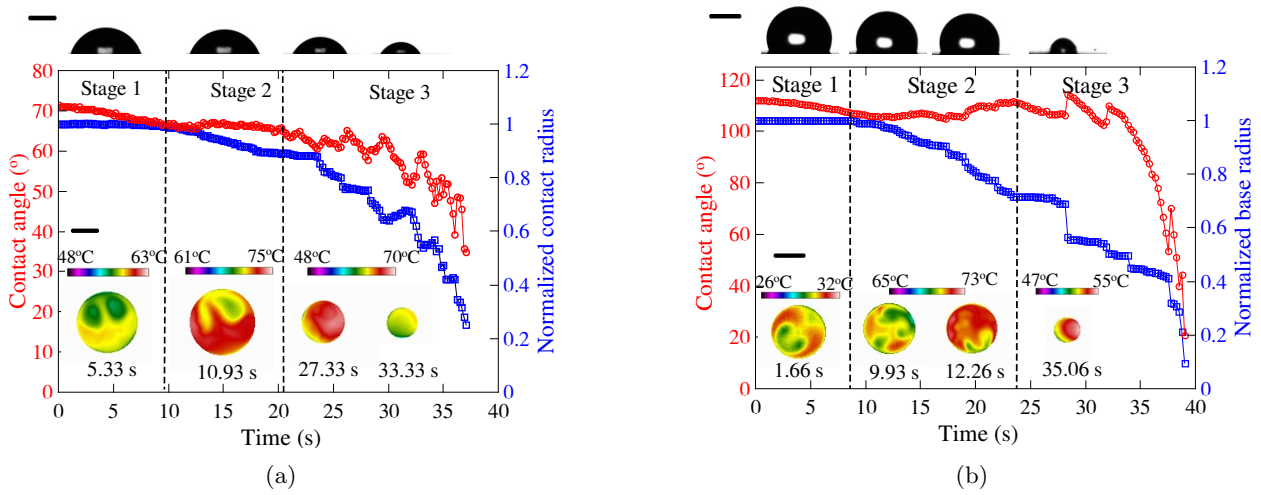

FIG. 4: Contact angle and normalized contact radius evolution on locally heated (a) hydrophilic and (b) hydrophobic surfaces. The three different evaporation stages can be readily identified by dashed lines. CCD snapshots from the side and IR thermography from the top are shown in insets. Scale bar is 1 mm.

face whereas on the hydrophobic surface the CCA mode is initially observed and thereafter transitions to stick-slip mode. The total evaporation time is observed to be smaller for drops on locally heated regime for both hydrophobic and hydrophilic cases. As shown in Fig. 9d in the Appendix, the higher substrate temperature should result in larger amount of heat supplied to the drops. Moreover, the estimation of the actual heat interactions of the drop is very complex, especially when considering the additional effect of the Marangoni flows and natural convection in the surrounding gas phase. For a more accurate estimation of the evaporation rates, numerical simulations to account for the continuous rise of the substrate temperature and for both convection within the drop and in the surroundings will be sought in the future.

The IR thermography images of temperature distribution on locally heated hydrophilic and hydrophobic substrates are presented in the insets of Fig. 4a and 4b (IR thermography movies for local heating on a hydrophilic and on a hydrophobic substrate are added in the accompanying supplementary material as videos SI.5 and SI.6, respectively [37]). On a hydrophilic surface, the initial temperature difference along the liquid-vapor interface results in the formation of the twin convective cells with the cold spot remaining virtually motionless in Stage 1. Whereas in Stage 2, an oscillatory azimuthal movement of the cold spot is observed. This shows that recirculatory flows are stronger in Stage 2 during the CCA mode. On the other hand, on a hydrophobic surface, twin convective cells emerge in Stage 1 and immediately move from one hemisphere to another creating an oscillatory merging and splitting of the cells, similar to previously reported phenomenon [4]. On a hydrophobic surface, convective flows are strong, whereas on a hydrophilic one the absence of strong oscillatory movement of the convective cells along the liquid-vapor interface is reported. On both hydrophilic and hydrophobic surfaces, towards the end of Stage 2, a visible instability in the movement of the convective cells is present, which leads to the observed temperature gradient across the liquid-vapor interface at the onset of Stage 3. As local heating results in more rapid and much higher substrate temperature, it is possible to also lead to stronger natural convection plume in the gas phase and hence the faster evaporation reported, similar to previous works [32, 33].

D. Variation of interfacial temperature difference (ΔT) in evaporating drops

The observed convective patterns presented above can be attributed to the temperature difference (ΔT) within each drop. In turn, ΔT arises from the difference between the hotter surface and the cooler drop combined with evaporative cooling and the thermal resistance of the drop. Careful analysis of the thermographic data allows us to quantify ΔT between the coldest and hottest point of the liquid-vapor interface (water is nearly opaque to the spectral range of our IR camera). The variation of ΔT is plotted in Fig. 5 as a function of time for all cases. An oscillation around a mean value which changes with time is readily apparent and arises due to the convective motion of hotter and colder fluid inside the drop (recirculation). In the case of uniformly heated substrates at 30 °C (Fig. 5a) an initial ΔT of ca. 2 °C is observed on the hydrophilic surface. As evaporation progresses, due to the comparatively lower evaporation rate at 30 °C, the temperature difference decreases continuously leading to an almost uniform temperature profile along the drop interface and within the drop. On a hydrophobic surface, an average temperature difference of ca. 2 °C is observed

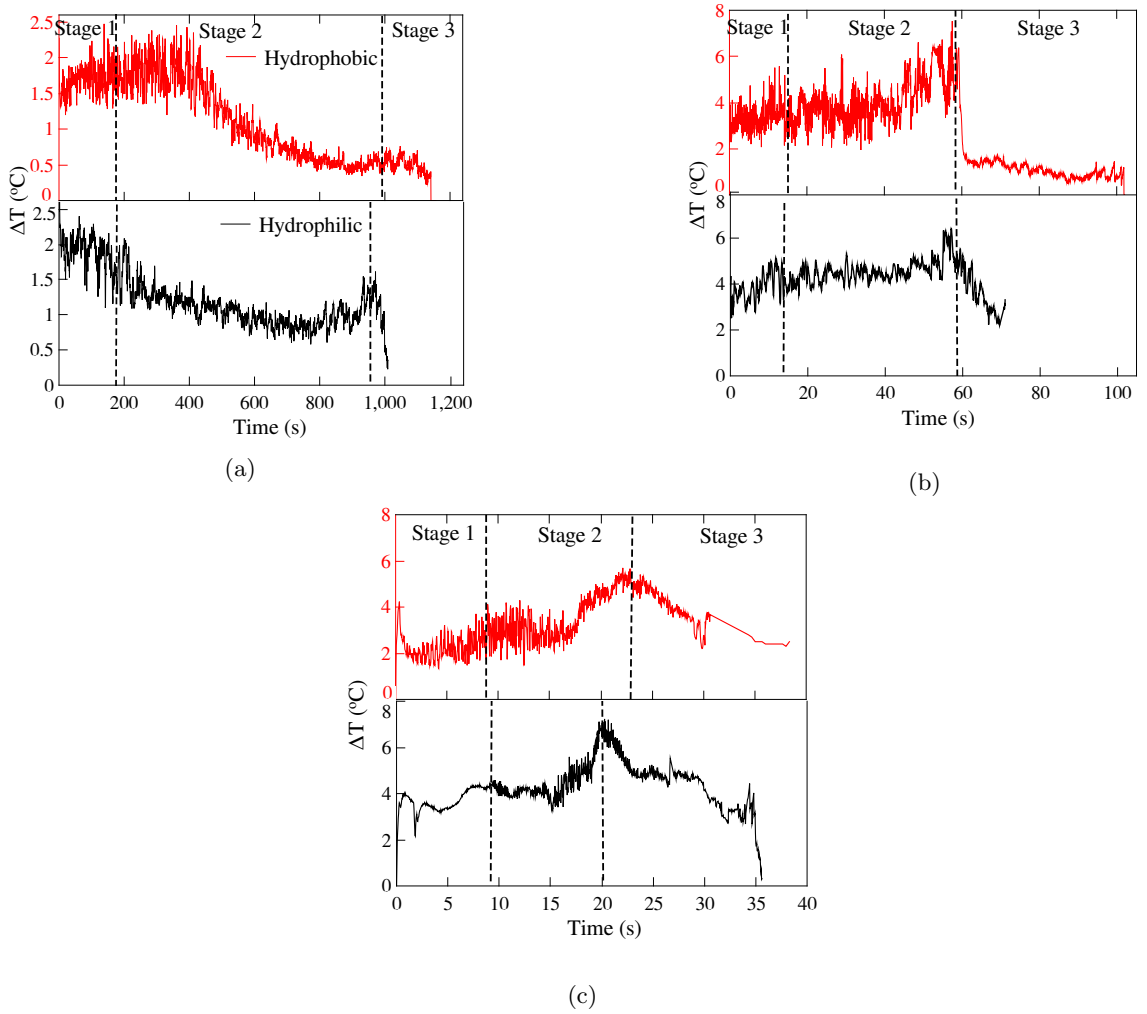

FIG. 5: Variation of interfacial temperature difference (ΔT) with time on uniformly heated substrates at (a) 30 °C, (b) 80 °C and (c) locally heated substrates. For each case, evolution on hydrophilic (black line) and hydrophobic (red line) surfaces is plotted.

for the initial 30 percent of the total evaporation time. The more uniform ΔT reported on a hydrophobic surface when compared to the continuously decreasing ΔT on the hydrophilic surface is reasoned due to the longer conduction path, i.e., drop height, on the hydrophobic case. As the substrate temperature is relatively low, ΔT decreases until an almost uniform temperature profile is observed [39].

At the high substrate temperature of 80 °C, ΔT variation with time is plotted in Fig. 5b for both hydrophilic and hydrophobic cases. It is interesting to note the clear distinguishing features of the evolution of ΔT with time which correlate with the three stages of the drop profile evaporation mentioned before in Figs. 3a and 3b. In Stage 1, as shown in Fig. 5b, the mean value of ΔT around which an oscillation can be observed, slightly increases with time, as the liquid near the hot contact line gets heated much faster than the liquid away from the contact line. We note here that during Stage 1, which follows CCR mode on both substrates, the contact area over which the heat is being supplied remains essentially constant. In Stage 2, the mean value around which ΔT oscillates remains almost constant at ca. 4 °C. This suggests that the drop attains a momentary thermal equilibrium between the heat supplied from the substrate and that released to the ambient due to evaporation and convection. Towards the end of Stage 2, a noticeable increase in ΔT which corresponds to the unstable movement of the convective cells is observed. After such increase, ΔT transitions into Stage 3 where a rapid decrease in contact angle causes the mixing of the liquid leading to a more homogeneous temperature distribution. These different aspects of the evolution of ΔT are qualitatively similar for both hydrophilic and hydrophobic surface, although on a hydrophobic substrate the drop in ΔT is much more pronounced than on the hydrophilic case due to the greater thermal resistance path across the drop, i.e., drop height.

Next, Figure 5c shows the evolution of ΔT over time for drops on locally heated substrates. Differences, when compared to the uniform heating cases, are evident. On a hydrophilic substrate, in Stage 1 ΔT increases right after the drop deposition to a value of ca. 4 °C. Thereafter, the recirculatory flows that manifest as twin vortices lower ΔT, which is in agreement with previous work [31]. Here also, the mean value of ΔT increases in Stage 1. Once the drop enters Stage 2, the mean value of ΔT remains constant in the beginning and increases rapidly until reaching a peak value of approximately 6 °C. This increase is more rapid compared to uniform heating at 80 °C. In Stage 3 of evaporation, ΔT slowly decreases. On the other hand, on a hydrophobic surface, in Stage 1 ΔT increases initially to a value of ca. 4 °C and twin vortices emerge. Eventually, evaporation enters Stage 2 and ΔT increases rapidly to a peak value higher than 6 °C, upon which point ΔT begins to decrease. Qualitatively, differences when comparing local heating case (Figure 5c) to uniformly heated cases at 80 °C (Figure 5b) are then evident. The qualitative behavior is then influenced by the different heating mode, i.e., constant heat flux and constant wall temperature heating conditions. This fundamental difference should greatly affect the evaporation kinetics, as we will show next. We should note here that curvature of the drops resting on the hydrophobic surfaces hinders observation of the temperature distribution close to the droplet base in contact with the substrate. To verify the validity of our top-view data, we conducted a number of side-view experiments and found good agreement within ±1°. For coherency, we only discuss the top-view data and provide an exemplary side view data comparison in the Supplementary Material [37].

E. Marangoni convection in evaporating pure water drops

To rationally understand the origin and to characterize the convective currents observed here, relevant non-dimensional numbers are calculated. Previously, the criterion of the ratio of dimensionless Rayleigh over Marangoni number for a liquid disk is proposed [40] and applied to evaporating drops to define the origin of convective flows [24]. Rayleigh number $Ra = \frac{g\beta H^4 \Delta T}{\nu \alpha R}$, Marangoni number $Ma = \frac{\gamma H^2 \Delta T}{\rho \nu \alpha R}$ and, Bond number $Bo = \frac{\rho g H^2}{\sigma}$ are calculated. Here, R and H are the characteristic radial and vertical drop length scales, respectively, σ is the surface tension, β is the thermal expansion coefficient, γ is the temperature coefficient of surface tension, ρ is the density, ν is the kinematic viscosity, and α is the thermal diffusivity for water at different temperatures. Average values of ΔT, R, and H for the whole period of evaporation are used in the calculation of the non-dimensional numbers. ΔT, Ma, Ra, Bo and ratio Ra/Ma are included in Table I. As the ratio of Ra/Ma is $<<1$, it can be concluded that the flows observed are Marangoni in origin. Additionally, Ra number is always less than the critical Ra number of 1000, hence Buoyant convection can be considered negligible [41]. When comparing Marangoni numbers for low and for high uniformly heated cases, Ma is much smaller at 30 °C compared to 80 °C, which is due to the lower temperature differences reported along the liquid-vapor interface. On another hand, when comparing ΔT on a hydrophobic substrate to that of a hydrophilic one, ΔT is lower on a hydrophobic substrate independently of the heating mode, i.e., uniform heating at 80 °C and local heating. This may seem counter-intuitive at first but considering the stronger recirculatory flows and resulting larger variations in ΔT around the mean value, lower average values of ΔT on hydrophobic surfaces are indeed expected. Nonetheless, the value of Ma which depends also on the geometric features of the drop is higher on a hydrophobic surface and implies the stronger emergence of Marangoni convection on hydrophobic surfaces.

TABLE I: Average of ΔT and relevant non-dimensional numbers for evaporating pure water drops.

Substrate type and temperature (°C)	ΔT (°C)	Ra	Ma	Bo	Ra/Ma
Uniform heating					
Hydrophilic, 30	1.33	13	701	0.07	0.01
Hydrophobic, 30	1.19	87	2594	0.11	0.03
Hydrophilic, 80	4.16	39	2740	0.08	0.01
Hydrophobic, 80	3.04	160	6300	0.14	0.02
Local heating					
Hydrophilic	4.14	56	3320	0.11	0.02
Hydrophobic	3.02	241	6736	0.22	0.03

Marangoni flow strength: To clearly delineate the effect of substrate wettability and type of heating on the presence of Marangoni convection, the Marangoni number for each of the evaporation stages (from Stage 1 to Stage 3) for all cases reported earlier is presented in Fig. 6. For a particular heating case, Ma is higher on a hydrophobic surface compared to a hydrophilic one independently of the evaporation stage. This clearly signifies the stronger Marangoni convection on hydrophobic surfaces. Another important aspect of Fig. 6 is that on uniformly heated substrates, i.e., 30 and 80 °C, Ma continuously decreases from Stage 1 to Stage 3, with higher Ma values at 80 °C. On the other hand, on locally heated substrates, an increase in Ma from Stage 1 to Stage 2 is observed followed by a decrease in Stage 3. Notably, the Ma value during stage 3 is higher for the local heating case when compared to uniform heating. The more uniform Ma reported during local heating throughout the complete evaporation is attributed to the continuous localized heat flux supplied to the drop when compared to the uniform heating case.

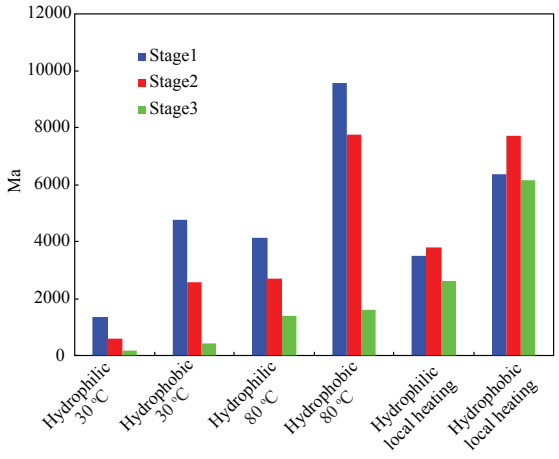

FIG. 6: Calculated Marangoni number during each stage of evaporation for different wettability and heating cases.

F. Evaporative flux

To give further insights on how substrate wettability and the heating modes influence the evaporation kinetics, the evaporative flux at the liquid-vapor interface with time for all the cases is plotted in Fig. 7 . Here, the evaporative flux is estimated as an average value over the entire liquid-vapor interface as $J = (\rho\frac{dV}{dt})/A_s$ where, ρ is liquid density, $\frac{dV}{dt}$ is the evaporation rate, $A_s = 2\pi RH$ is the liquid-vapor interface area of the drop with R and H as the radius and height of the drop, respectively. Such approximation is rather reasonable since our drops exhibit initial contact angles close to 90° at which diffusion along the liquid-vapor interface can be considered uniform [9]. As expected, heating the substrate enhances the magnitude of the evaporative flux (Fig. 7a and 7b). For uniform heating, the evaporative flux remains almost constant in Stages 1 and 2 independently of the substrate wettability. The onset of Stage 3 coincides with a steep increase in the evaporative flux. This sudden increase in the evaporative flux may cause the momentary increase in liquid motion within the drop resulting in further internal mixing and more homogeneous temperature differences, which is supported by the decrease in ΔT. In the locally heated case, the evaporative flux is evidently different as shown in Fig. 7c. In this case, the evaporative flux increases continuously since the beginning of the evaporation, opposed to the almost constant evaporative flux reported on uniformly heated substrates. Notably, the value of J at the onset of Stage 3 (indicated by arrows) is much higher than for uniform heated case. Under local heating, both the continuous local heat flux bringing the substrate temperature above 100 °C (see Fig. 9 in Appendix) and the stronger natural convective plume in the gas phase leads to the greater evaporation rates reported [32, 33]. This is a clear difference between heating modes on the evaporation kinetics.

G. Vapor diffusion model

Vapor diffusion models of drop evaporation are revisited to study the effect of Marangoni convection on the evolution of volume with time. The free evaporation of a water drop is limited by the diffusion of vapor to the immediate surroundings. In the present study, the time scale for vapor diffusion $R^2/D \approx 0.03$ is much lower than the total evaporation time even at higher substrate temperatures. Thus, the evaporation process can be thought of as a quasi-steady process where the rate-limiting step is vapor diffusion to the ambient. Then, the evolution of volume with time is calculated using the vapor diffusion model proposed by Popov [42]. For the estimation of the saturated vapor concentration at the drop interface, the average liquid-vapor interface temperature obtained from IR thermography is used as opposed to the substrate temperature adopted in the earlier studies [43, 44].

Popov [42] reported the exact solution of Laplace equation governing the vapor diffusion process in toroidal coordinates. This solution considers the non-uniformity of evaporation flux at the liquid-vapor interface thereby can be applied for a whole range of initial contact angles (0° to 180°). The rate of mass loss of a sessile drop can be written as,

$$\frac{dm}{dt} = \rho\frac{dV}{dt} = -\pi RD\left[c_s\left(T_s\right) - c_s\left(T_a\right)\right] f\left(\theta\right), \qquad (1)$$

$$f\left(\theta\right) = \frac{\sin\theta}{1+\cos\theta} + 4\int_0^\infty \frac{1+\cosh 2\theta\tau}{\sin 2\pi\tau}\tanh\left[\left(\pi-\theta\right)\tau\right]d\tau \qquad (2)$$

Here, T_s is the average liquid-vapor interface temperature and T_a is the ambient temperature. The complex integral in Eq. 2 is solved using numerical integration in MATLAB. Using spherical cap assumption, the mass of a drop with contact radius R and contact angle θ can be written as,

$$m = \frac{\pi\rho R^3}{3g\left(\theta\right)}; g\left(\theta\right) = \frac{\sin^3\theta}{\left(1-\cos\theta\right)^2\left(2+\cos\theta\right)} \qquad (3)$$

Writing R in terms of volume from Eq. 3, the expression for evaporative mass loss in Eq. 1 can be written as,

$$\rho\frac{dV}{dt} = -\pi\left(\frac{3}{\pi}Vg\left(\theta\right)\right)^{1/3} D\left[c_s\left(T_s\right) - c_s\left(T_a\right)\right] f\left(\theta\right) \qquad (4)$$

The change in contact angle when the drop evaporates in CCR mode (R_c is radius in CCR mode) can be obtained from Eqs. 1 and 4 as,

$$\frac{d\theta}{dt} = \frac{-D\left(c_s\left(T_s\right) - c_s\left(T_a\right)\right)}{\rho R_c^2}\left(1+\cos\theta\right)^2 f(\theta) \qquad (5)$$

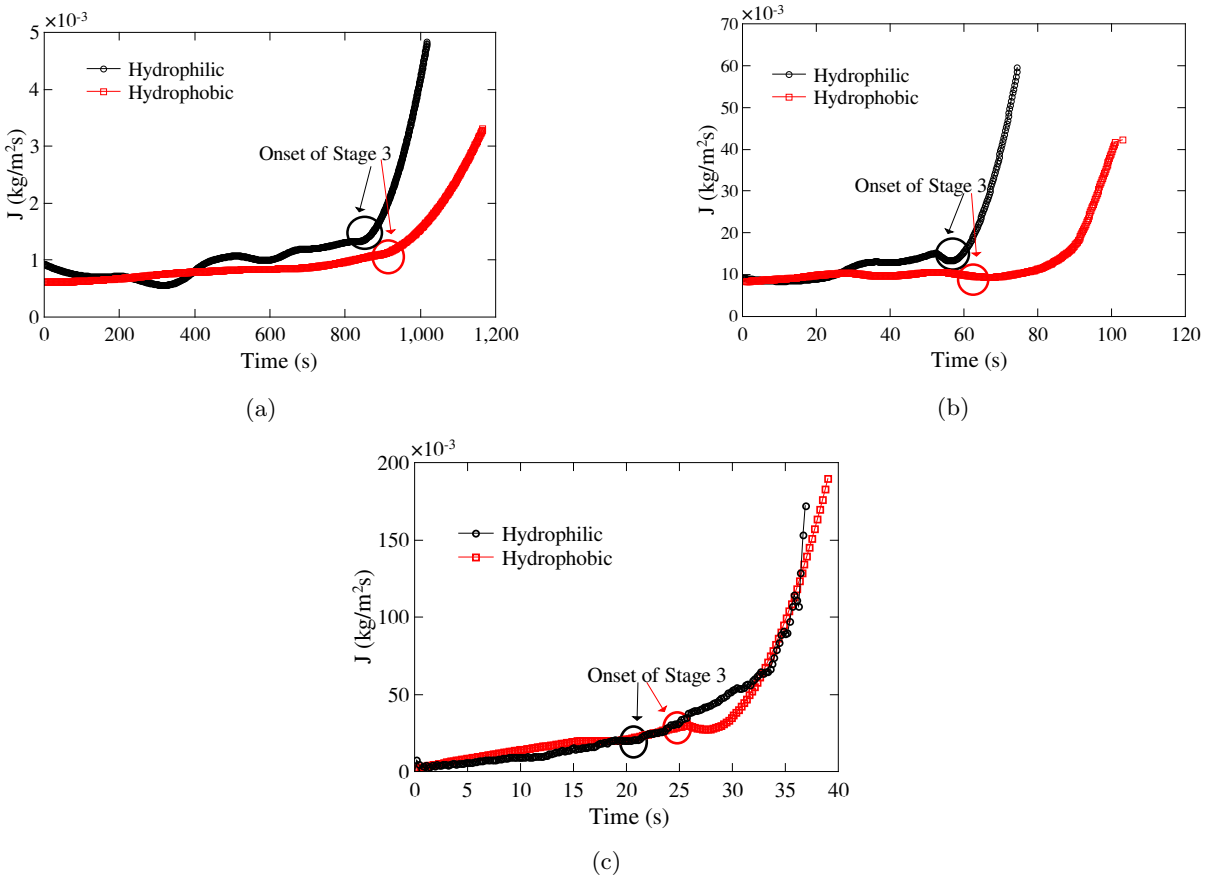

FIG. 7: Variation of evaporative flux J, (kg m^{-2} s^{-1}), with time, t (seconds), on uniformly heated substrates at (a) 30 °C, (b) 80 °C and (c) locally heated substrates. For each case, evolution on hydrophilic (black line) and hydrophobic (red line) surfaces is plotted. Arrows indicate the onset of Stage 3 of evaporation.

Numerically integrating Eq. 5 gives the variation of θ with time in CCR mode. Using R_c and θ, the volume of drop evaporating in CCR mode can be obtained as,

$$V = \frac{\pi R_c^3}{3g\left(\theta\right)} \tag{6}$$

During the CCA mode, the square of contact radius decreases linearly and volume of the drop at any time during evaporation can be written by integrating Eq. 4 as,

$$V^{2/3} = V_i^{2/3} - \frac{2\pi D\left(c_s\left(T_s\right) - c_s\left(T_a\right)\right)}{3\rho}\left(\frac{3}{\pi}\right)^{1/3} \left(g\left(\theta_c\right)\right)^{1/3} f(\theta_c)t, \tag{7}$$

where, θ_c is the contact angle in CCA mode.

The experimental evolution of drop residual volume with time is compared with the prediction of Popov model using Eqs. 6 and 7. This comparison is presented in Fig. 8 for drops on uniformly heated substrates at 30 °C (Fig. 8a) and at 80 °C (Fig. 8b) and on locally heated substrates (Fig. 8c). In all reported cases, an over-prediction in the total evaporation time compared to the experimental evaporation time is observed. This under-prediction on the evaporation rate by the diffusion model is reasoned due to the dominant presence of Marangoni convection inside the drop. Further, enhancement of evaporation rate due to natural convection in ambient during evaporation has been recently reported [32–35]. To account for the presence of natural convection in the gas phase, the non-dimensional Grashof number which indicates the strength of buoyancy is estimated as $Gr = \frac{g\Delta\rho R^3}{{\nu_g}^2\rho_g}$. Here, g is the acceleration due to gravity, R is the initial drop radius, ν_g is kinematic viscosity and ρ_g is the density of ambient air. $\Delta\rho$ is the net density difference causing the flow [35]. Calculated Gr values for the present experimental conditions are in the range of 12 to 15. The value of Gr confirms the presence of buoyancy driven natural convection induced by the difference in air density. Nonetheless, the relatively low Gr values compared to previous studies [32–35], highlight that buoyancy driven natural convection cannot be the sole reason for the observed enhancement on the evaporation rate. When looking into buoyancy driven natural convection under local heating and uniform heating,

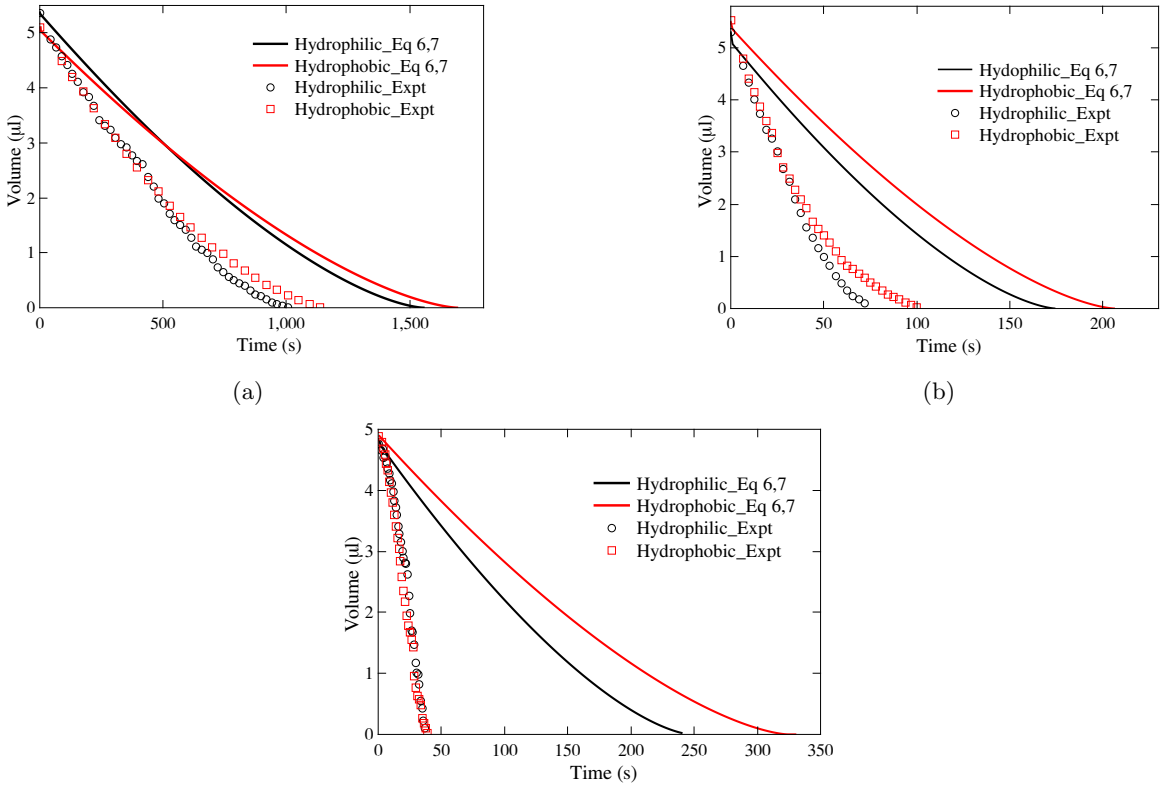

FIG. 8: Volume evolution with time for drops on uniformly heated substrates at (a) 30 ˚C, (b) 80 ˚C and (c) locally heated substrates. The lines represent the volume obtained from diffusion model by Popov [42] using Eqs. 6, 7 and symbols represent experimental values.

small differences on the Gr numbers are reported, i.e. Gr number for local heating is 125% greater than that of uniform heating. Whereas when looking into Marangoni convection, Ma numbers at the later stage of evaporation are found to be up to 300% greater for the local heating case when compared to the uniform case. Therefore, both Marangoni convection and buoyancy driven natural convection are put forward as the main mechanisms for the increased evaporation rates reported in the present experiments. If we consider t as the total time taken for evaporation, the absolute relative deviation in the total evaporation time when comparing the diffusion model and experiments can be estimated as $\frac{t_{experiment}-t_{diffusion}}{t_{experiment}}$. For the cases of uniformly heated substrates at 30 ˚C, there is a 50% over prediction of the evaporation time. Whereas at 80 ˚C, where significant Marangoni convection is present, the absolute relative deviation is almost 100% (see Figs. 8a and 8b). On similar lines, as shown in Fig. 8c, a great over-prediction of the total evaporation time is observed for locally heated substrates. The dominant presence of Marangoni convection reported here eases the evaporation process increasing the evaporation rate [45, 46]. Previous studies calculated the vapor concentration at liquid-vapor interfaces at the substrate temperature [43, 44]. However, evaporative cooling and Marangoni recirculation should lower the liquid-vapor interface temperature to a value lower than that of the substrate. We must note here that in the present study calculating the vapor concentration at the substrate temperature rather than using that at the liquid-vapor interface for drops on uniformly heated substrates could not explain the total evaporation rate enhancement reported. This highlights that the diffusion driven model merits improvement in the future to account for the nonuniform temperature distribution at the liquid-vapor interface arising from the Marangoni convection within the liquid and the buoyancy driven natural convection in the gas phase. At this stage it is difficult to decouple the effect of Marangoni convection within the drop and buoyancy driven natural convection in the gas phase on the heat and mass transfer of drops on both uniform and locally heated substrates. Hence, future work will sought the design of the appropriate experimental conditions that can decouple such phenomena.

IV. CONCLUSION

We report a systematic study on two parameters affecting the emergence of Marangoni convection patterns within pure water drops and how these patterns influence the evaporation kinetics of the drops. In particular, we successfully induced Marangoni flows under two different heating regimes, i.e. constant wall temperature and constant heat flux, and found the constant heat flux or locally heated case to have a detrimental effect on both the observed Marangoni flows and the shortening of the evaporation rates. In addition, we determined that hydrophobicity plays a major role in the emergence of the Marangoni flows and the coupled evaporation kinetics. More importantly, heating the substrates led to much higher evaporation rates than those expected by established diffusion models. We attributed this enhancement to a combination of Marangoni flows within the liquid and natural convection of the vapor phase to the ambient. We believe our findings to elucidate the physical mechanism of drop evaporation on heated surfaces, beneficial to numerous applications from spray cooling to colloidal deposition in bio medical diagnosis systems or ink-jet printing.

ACKNOWLEDGMENTS

A.P. acknowledges the support received by the Japanese Society for the Promotion of Science (JSPS). D.O., A.A., S.H. and Y.T. acknowledge the support of the International Institute for Carbon-Neutral Energy Research (WPI-I2CNER). D.O. acknowledges the support received by the JSPS KAKENHI (Grant No. JP16K18029). T.J. acknowledges Dept. of Mechanical Engineering., IIT Madras for providing the financial support in building a part of experimental setup.

Appendix: Numerical simulation of local heating case

Numerical simulations are performed in COMSOL 5.2 considering only the substrate with localized heat source. The dimensions of silicon substrate and (10mm×10mm×0.5mm), glass slides below the substrate (50mm×40mm×1mm) are those measured from the experiments. The numerical domain is shown in Fig. 9a. Initially, the temperature is 17 °C (ambient experimental conditions) throughout the numerical domain. The bottom surface of the glass slide supporting the silicon substrate is considered considered as an insulated boundary condition. Heat flux with convective heat transfer coefficient of 8 W/m^{2}K is considered for all the boundaries except the bottom surface of glass supports. The laser heat input is considered as a point source with 1.8 W and a heat source radius of 0.15 mm. Transient heat transfer is studied and temperature distribution on the wafer is studied up to a period of 40 s. The temperature profile at 5 s and 10 s are shown in Figs. 9b and 9c, respectively. The temperature profile clearly shows a non-uniform temperature distribution across the substrate, in agreement with the experimental hot-spot. Further, the temperature rise (solid line) of the hot-spot is shown in Fig. 9d for a period of 40 s, which appears to correlate well with the experimental data (circles).

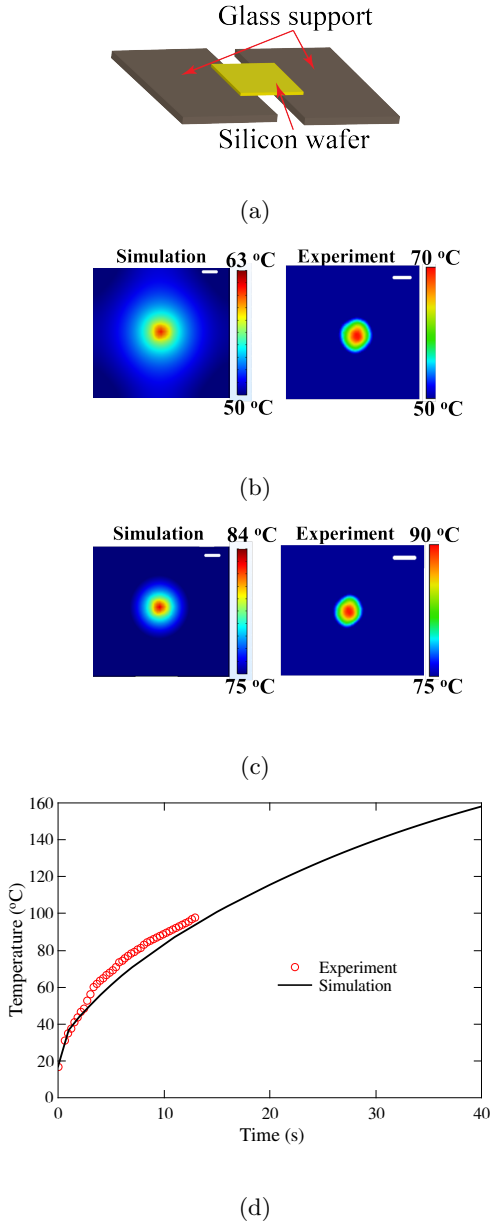

FIG. 9: Numerical simulation performed for locally heated substrates without drop. (a) geometry, temperature profile on substrate from numerical simulation and experiment at (b) 5, (c)10 s. Scale bar indicates 1 mm. (d) comparison of temperature at center of heating spot from experiment and simulation

[1] Paul Calvert, Chemistry of Materials **13**, 3299 (2001).
[2] T. S. Wong, T. H. Chen, X. Shen, and C. M. Ho, Analytical Chemistry **83**, 1871 (2011).
[3] D. Xia and S. R. J. Brueck, Nano Letters **8**, 2819 (2008).
[4] A. Askounis, Y. Takata, K. Sefiane, V. Koutsos, and M. E. R. Shanahan, Langmuir **32**, 4361 (2016).
[5] W. Jia and H. H. Qiu, Experimental Thermal and Fluid Science **27**, 829 (2003).
[6] R. G. Picknett and R. Bexon, Journal of Colloid And Interface Science **61**, 336 (1977).
[7] K. Birdi and D. Vu, Journal of Adhesion Science and Technology **7**, 485 (1993).
[8] M. E. R. Shanahan, K. Sefiane, and J. R. Moffat, Langmuir **27**, 4572 (2011).
[9] S. Dash and S. V. Garimella, Langmuir **29**, 10785 (2013).
[10] S. M. M. Ramos, J. F. Dias, and B. Canut, Journal of Colloid and Interface Science **440**, 133 (2015).
[11] D. Orejon, K. Sefiane, and M. E. R. Shanahan, Langmuir **27**, 12834 (2011).
[12] E. Y. Gatapova, A. A. Semenov, D. V. Zaitsev, and O. A. Kabov, Colloids and Surfaces A: Physicochemical and Engineering Aspects **441**, 776 (2014).
[13] P. J. Sáenz, A. W. Wray, Z. Che, O. K. Matar, P. Valluri, J. Kim, and K. Sefiane, Nature Communications **8**, 14783 (2017).
[14] Y. Fukatani, D. Orejon, Y. Kita, Y. Takata, J. Kim, and K. Sefiane, Physical Review E **93(4)**, 043103 (2016).
[15] A. Askounis, K. Sefiane, V. Koutsos, and M. E. R. Shanahan, Colloids and Surfaces A: Physicochemical and Engineering Aspects **441**, 855 (2014).
[16] K. Sefiane, S. K. Wilson, S. David, G. J. Dunn, and B. R. Duffy, Physics of Fluids **21** (2009).
[17] G. J. Dunn, S. K. Wilson, B. R. Duffy, S. David, and K. Sefiane, Journal of Fluid Mechanics **623**, 329 (2009).
[18] S. David, K. Sefiane, and L. Tadrist, Colloids and Surfaces A: Physicochemical and Engineering Aspects **298**, 108 (2007).
[19] H. Hu and R. G. Larson, Journal of Physical Chemistry B **106**, 1334 (2002).
[20] J. M. Stauber, S. K. Wilson, B. R. Duffy, and K. Sefiane, **31**, 3653 (2015).
[21] J. J. Hegseth, N. Rashidnia, and A. Chai, Physical Review E **54**, 1640 (1996).
[22] H. Hu and R. G. Larson, Journal of Physical Chemistry B **110**, 7090 (2006).
[23] R. D. Deegan, O. Bakajin, T. F. Dupont, G. Huber, S. R. Nagel, and T. A. Witten, Nature **389**, 827 (1997).
[24] K. Sefiane, J. R. Moffat, O. K. Matar, and R. V. Craster, Applied Physics Letters **93(7)**, 074103 (2008).
[25] D. Brutin, B. Sobac, F. Rigollet, and C. Le Niliot, Experimental Thermal and Fluid Science **35**, 521 (2011).
[26] K. Sefiane, A. Steinchen, and R. Moffat, Colloids and Surfaces A: Physicochemical and Engineering Aspects **365**, 95 (2010).
[27] A. Chandramohan, S. Dash, J. A. Weibel, X. Chen, and S. V. Garimella, Langmuir **32**, 4729 (2016).
[28] X. Xu and J. Luo, Applied Physics Letters **91(12)**, 124102 (2007).
[29] N. D. Patil, P. G. Bange, R. Bhardwaj, and A. Sharma, Langmuir **32**, 11958 (2016).
[30] Y. Kita, A. Askounis, M. Kohno, Y. Takata, J. Kim, and K. Sefiane, Applied Physics Letters **109** (2016), 10.1063/1.4966542.
[31] A. Askounis, Y. Kita, M. Kohno, Y. Takata, V. Koutsos, and K. Sefiane, Langmuir **33**, 5666 (2017).
[32] P. L. Kelly-Zion, C. J. Pursell, S. Vaidya, and J. Batra, Colloids and Surfaces A: Physicochemical and Engineering Aspects **381**, 31 (2011).
[33] F. Carle, B. Sobac, and D. Brutin, Applied Physics Letters **102** (2013), 10.1063/1.4792058.
[34] S. Dehaeck, A. Rednikov, and P. Colinet, Langmuir **30**, 2002 (2014).
[35] S. Somasundaram, T. N. C. Anand, and S. Bakshi, Physics of Fluids **27** (2015), 10.1063/1.4935355.
[36] *MATLAB Reference Manual* (The MathWorks Inc., Natick, Massachusetts, 2016).
[37] See Supplementary Material for videos of thermal patterns recorded using IR camera.
[38] S. W. Paik, K. D. Kihm, S. P. Lee, and D. M. Pratt, Journal of Heat Transfer **129**, 966 (2006).
[39] G. Fabien, M. Antoni, and K. Sefiane, Langmuir **27**, 6744 (2011).
[40] N. Garnier, A. Chiffaudel, and F. Daviaud, Dynamics of Spatio-Temporal Cellular Structures: Henri Benard Centenary Review **207**, 147 (2006).
[41] F. Duan and C. A. Ward, Langmuir **25**, 7424 (2009).
[42] Y. O. Popov, Physical Review E **71(3)**, 036313 (2005).
[43] S. Dash and S. V. Garimella, Physical Review E **89(4)**, 042402 (2014).
[44] B. Sobac and D. Brutin, Langmuir **27**, 14999 (2011).
[45] P. Chen, S. Harmand, S. Ouenzerfi, and J. Schiffler, Journal of Physical Chemistry B **121**, 5824 (2017).
[46] K. Sefiane, Y. Fukatani, Y. Takata, and J. Kim, Langmuir **29**, 9750 (2013).